Second-order wave loads on floating wind parks with shared mooring

Journal of Physics: Conference Series **2626** (2023) 012038 doi:10.1088/1742-6596/2626/1/012038

Second-order wave loads on floating wind parks with shared mooring

Thomas Sauder
SINTEF Ocean - Trondheim - Norway
NTNU - Department of Marine Technology - Trondheim - Norway
E-mail: thomas.sauder@sintef.no

Abstract. Wave loads on lattices of marine structures, such as wind parks with shared mooring systems, are considered. Modal excitation induced by second-order low-frequency wave loads is derived, leading to modal quadratic transfer functions. The consequence for the modal loads, of applying Newman's approximation is investigated.

1. Introduction

Forthcoming generations of offshore power grids might be largely floating and composed of hundreds of subsystems harvesting, converting and storing energy. As an example, floating wind parks, currently in the multi-MW power range, might eventually reach a multi-GW capacity, and be combined with e.g. floating photovoltaic cells, and hydrogen production units. In this context, offshore energy installations might change character, from single moored floating structures to large *lattices* of floating structures.

Lattices are here defined as two-dimensional arrangements of identical structures, interconnected by soft connections such as mooring lines. As the size of the lattice increases, the number of eigenmodes and the range of associated eigenfrequencies will increase, with many possible resonances in the low-frequency (LF) range, i.e. below the wave-frequency range. When operating near these frequencies, it is critical to quantify the excitation forces and the amount of damping in the system to detect possible resonance, and accurately estimate responses of interest for the lattice. LF excitation loads are mainly due to wind and waves. The present paper focuses on the latter. LF wave loads result from nonlinear interactions between frequency components in the wave spectrum, and between the waves and a moving structure. Difference-frequency quadratic transfer functions (QTFs) have traditionally been used to describe these effects on individual floaters.

Several authors have investigated the behaviour of lattices of floating wind turbines. Static analyses [1, 2, 3], eigenvalues analyses [4] and dynamic time-domain analyses [5, 6, 7, 8, 9] at various fidelity levels have been reported. However, no frequency-domain study targeting specifically nonlinear wave loads has been carried out yet. Frequency domain approaches, despite their limitations when considering nonlinear systems, often yield a good understanding of the physical phenomena at play.

The main contribution of the paper is a derivation of the modal excitation from second-order (LF) wave loads, and of the lattice response under simplifying assumptions. The consequence of

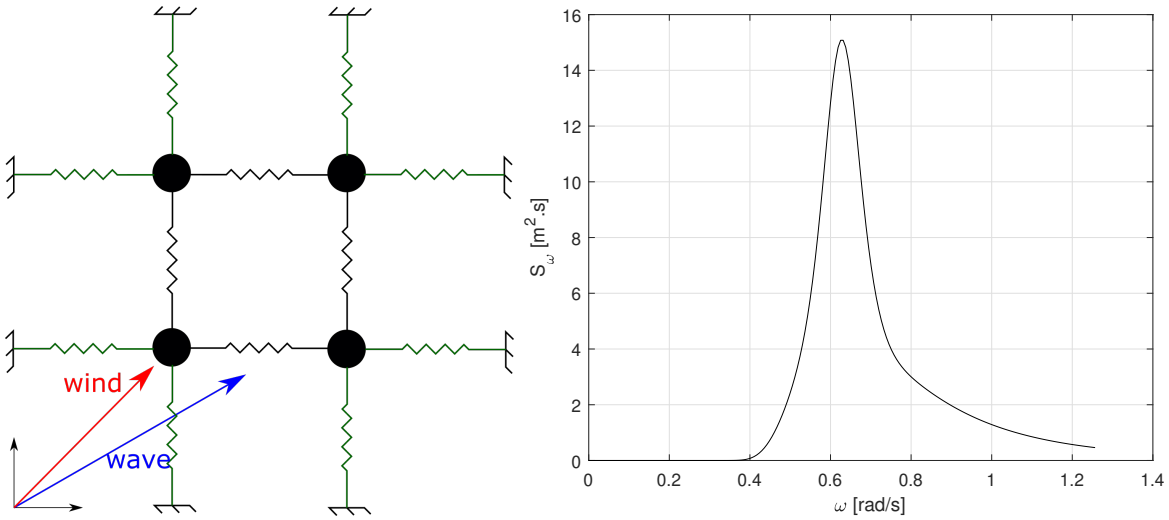

Figure 1. Left: grid type of lattice that will be considered in the present study (N=2). Anchored lines (represented in green) have a length and stiffness denoted l_a and k_a, respectively. Shared lines (represented in black) have a length and stiffness denoted l_s and k_s respectively. Right: wave spectrum used in the example: JONSWAP spectrum with $H_s = 7$m, $T_p = 10$s and γ=3.3

Table 1. Lattice parameters

Notation and value	
$N = 2$	number of FWTs on one row of the lattice
$m = 14175 + 8300$ t	mass (mass + asymptotic LF added mass) of each FWT
$k_s = 60$ kN/m	linear stiffness of the shared lines
$k_a = 120$ kN/m	linear stiffness of the anchored lines
$l_s = 1260$ m	projected length on waterplane of the shared lines
$l_a = 726$ m	projected length on waterplane of the anchored lines
$T_0 = 950$ kN	pre-tension of the lines
$\gamma_1 = 5 \times 10^{-3}$ s^{-1}	mass coefficient of the Rayleigh damping
$\gamma_2 = 3 \times 10^{-1}$ s	stiffness coefficient of the Rayleigh damping

using Newman's approximation instead of a full QTF is also investigated. Theory is presented in Sections 3 to 7, illustrated by an example introduced in Section 2.

2. Example case

The example case is similar to the one studied by Connolly in [4]. A grid type of lattice is defined, as illustrated in Figure 1. The mooring lines are approximated by a linear stiffness with values taken from [4] and recapped in Table 2. The pre-tension in the mooring lines is 950 kN. The mass and LF asymptotic added mass properties for the floater correspond to the INO WINDMOOR 12MW design [10]. For this floater, a numerical QTF estimate is available, see Figure 5. The behaviour of the lattice will be investigated in a sea-state described by the JONSWAP spectrum $S(\omega)$, and characterized by a significant wave height $H_s = 7$ m and a peak period of $T_p = 10$ s, see Figure 1. The wave propagation direction is $\beta = 30^o$ with respect to the horizontal axis. Static wind loads are represented by a constant force of 1.5 MN, applied on all four floaters with an angle of 45^o with respect to the horizontal axis.

3. Eigenmodes

We consider the general case of a lattice with n_d degrees of freedom. In the example case, only surge and sway motions are included for simplicity, so that $n_d = 2N^2$. Let us denote $r \in \mathbb{R}^{n_d}$ the lattice response to an external nodal excitation $F \in \mathbb{R}^{n_d}$. Dynamic equilibrium yields

$$M\ddot{r} + C\dot{r} + Kr = F \tag{1}$$

where M, C and K are $n_d \times n_d$ mass, damping and stiffness matrices. The response is defined relative to the equilibrium configuration.

Note that system matrices for a statically loaded lattice can be very different from their counterpart obtained in an unloaded scenario due to large deformations under external static loading. In that case, the equilibrium configuration and the values of these matrices must be calculated with a nonlinear static analysis, which has been done here.

Free vibrations of the lattice at a frequency ω are described by

$$(-M\omega^2 + K)r = 0 \tag{2}$$

Assume that M is a real symmetric positive-definite matrix. M can be Cholesky-decomposed as a product $M = LL^*$ where L is a lower triangular matrix and * denotes the Hermitian transpose. Defining $q = L^*r$, free vibration can then be re-written as

$$\tilde{K}q = \omega^2 q \tag{3}$$

where

$$\tilde{K} = L^{-1}K(L^*)^{-1} \tag{4}$$

is a symmetric matrix. Then, there exist a set of eigenvectors $(\phi_i)_{i\in\{1...n_d\}}$ of $\tilde{K}$ that form an orthonormal[1] basis of the Euclidean vector space $\mathbb{R}^{n_d}$. Each ϕ_i is associated to an eigenvalue Ω_i^2. We define

$$\Phi = [\phi_1, ..., \phi_{n_d}] \tag{5}$$

and

$$\Lambda = diag(\Omega_1^2, ..., \Omega_{n_d}^2) \tag{6}$$

so that

$$\tilde{K}\Phi = \Lambda\Phi \tag{7}$$

Orthonormality yields $\Phi^*\Phi = I$.

Note that all Ω_i are not necessarily distinct. In our example, when no mean load is applied to the lattice, several modeshapes are associated with the same eigenfrequency (*degenerate* eigenmodes), as shown in Figure 2. It is still possible in that case to define an orthonormal basis Φ using Gram-Schmidt orthogonalization. In the case of an arbitrarily loaded lattice, eigenmodes are in general non-degenerate, i.e. that all eigenfrequencies are distinct, as shown in Figure 3.

[1] In case of non-degenerate eigenmodes (all eigenvalues are distinct), orthogonality of eigenvectors is proved as follows. Let $u \in \{1, ..., n\}$. $\omega_u^2\phi_u = \tilde{K}\phi_u$, $\omega_u^2\phi_u^* = (\tilde{K}\phi_u)^*$, $\tilde{K}$ being real symmetric we have $\omega_u^2\phi_u^* = \phi_u^*\tilde{K}$. Let $v \in \{1, ..., n\}$. Post multiplying by ϕ_v, we have $\omega_u^2\phi_u^*\phi_v = \phi_u^*\tilde{K}\phi_v$, i.e. $\omega_u^2\phi_u^*\phi_v = \phi_u^*\omega_v^2\phi_v$, yielding $(\omega_u^2 - \omega_v^2)\phi_u^*\phi_v = 0$. So if $u \neq v$, then ϕ_u and ϕ_v are orthogonal. They can be normalized to yield an orthonormal basis.

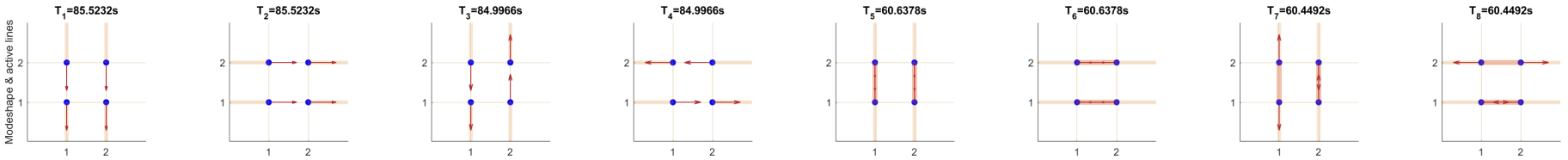

Figure 2. Modeshapes and associated eigenperiods for an unloaded 2x2 lattice. Red arrows indicate the nodal displacement for each mode. Segments of varying red color intensity represent the tension in each of the anchored and shared lines for the given mode (based on relative nodal displacements).

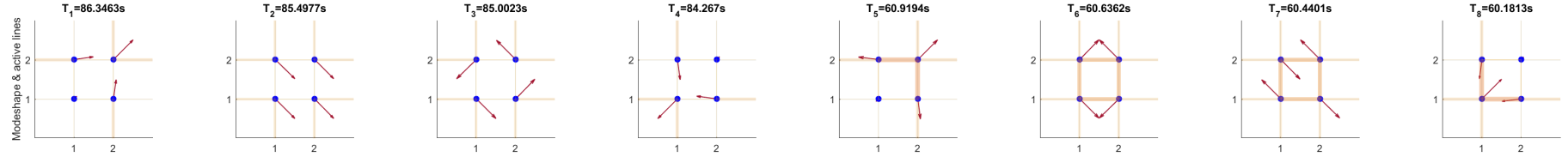

Figure 3. Same representation of eigenmodes as in Figure 2, but resulting from a nonlinear static analysis, and where all nodes have been loaded with an 1.5MN force applied with a 45^o angle with respect to the x-axis.

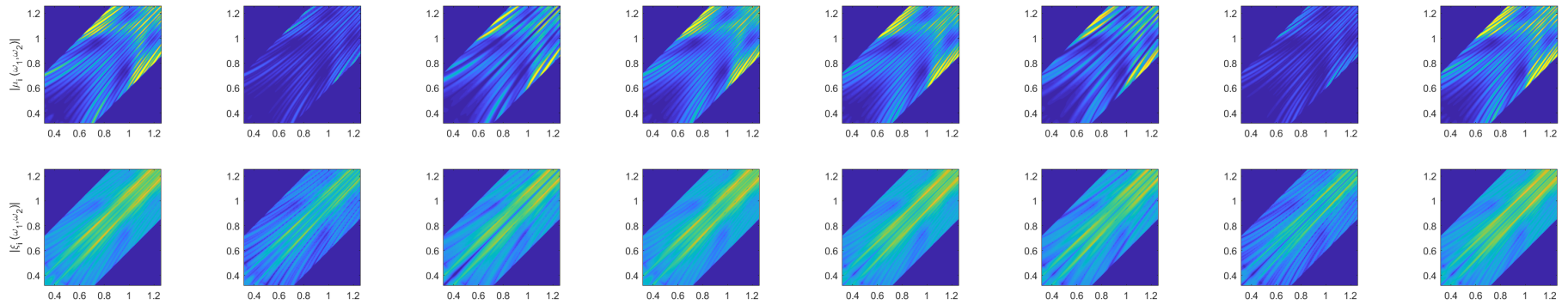

Figure 4. Modal loads (top) and responses (bottom) in a bi-chromatic wave field with frequency ω_1 (x-axis) and ω_2 (y-axis). Each column correspond to the eigenmodes from Figure 3 above. The colorbar is similar to Figure 5: the blue color corresponds to relatively small levels, and yellow color to relatively large levels.

4. Modal load and response

The modal load vector $\mu \in \mathbb{R}^{n_d}$ and the modal response vector $\xi \in \mathbb{R}^{n_d}$ are defined by

$$\mu = \Phi^* L^{-1} F \tag{8}$$

$$\xi = \Phi^* L^* r \tag{9}$$

The dynamic equilibrium (1) can be rewritten as $M(L^{-1})^*\Phi\ddot{\xi}+C(L^{-1})^*\Phi\dot{\xi}+K(L^{-1})^*\Phi\xi = L\Phi\mu$. Premultiplying by L^{-1}, leads to $\Phi\ddot{\xi} + L^{-1}C(L^{-1})^*\Phi\dot{\xi} + \tilde{K}\Phi\xi = \Phi\mu$. Premultiplying by Φ^*, we get $\ddot{\xi} + \Phi^*L^{-1}C(L^{-1})^*\Phi\dot{\xi} + \Phi^*\tilde{K}\Phi\xi = \mu$, and obtain the modal system of differential equations:

$$\ddot{\xi} + \Phi^*L^{-1}C(L^{-1})^*\Phi\dot{\xi} + \Lambda\xi = \mu \tag{10}$$

where couplings between the modes exist due to the modal damping term. To proceed with the analysis, it is practical to assume Rayleigh damping, even if there is no indication that this assumption is fulfilled in reality. In that case,

$$C = \gamma_1 M + \gamma_2 K \tag{11}$$

yielding $L^{-1}C(L^{-1})^* = \gamma_1 L^{-1}M(L^{-1})^* + \gamma_2 L^{-1}K(L^{-1})^* = \gamma_1 I + \gamma_2\tilde{K}$. Then $\ddot{\xi} + \Phi^*(\gamma_1 I + \gamma_2\tilde{K})\Phi\dot{\xi} + \Lambda\xi = \mu$, which leads to an *uncoupled* system of differential equations:

$$\forall i \in \{1, ..., n_d\}, \ddot{\xi}_i + (\gamma_1 + \gamma_2\Omega_i^2)\dot{\xi}_i + \Omega_i^2\xi_i = \mu_i \tag{12}$$

In that case, the complex modal response $\bar{\xi_i}$ to a harmonic modal load $\bar{\mu_i}$ at frequency Ω can immediately be found by

$$\forall i \in \{1, ..., n_d\}, \bar{\xi_i} = \frac{\bar{\mu_i}}{\Omega_i^2 - \Omega^2 + i\Omega(\gamma_1 + \gamma_2\Omega_i^2)} \tag{13}$$

Nodal responses and loads can be recovered from their modal counterparts by

$$r = (L^{-1})^*\Phi\xi \tag{14}$$

$$F = L\Phi\mu \tag{15}$$

5. Second-order modal wave loads and response

Consider now a lattice in an incident multi-chromatic wave field $\Re\left[\sum_j \zeta_j e^{i\omega_j t - k_j u\cdot x}\right]$, where $\zeta_j \in \mathbb{C}$ describes the amplitude of the wave component and its phase at origin, k_j the associated wave number, $u = (\cos\beta, \sin\beta)^\top$ is he wave propagation direction, and x the position vector. The second-order wave load at a frequency $\Delta\omega \geq 0$ on a floater located at x, and on the degree of freedom $d \in \{1, 2, 6\}$ (for surge, sway and yaw) is given by

$$f_d(\Delta\omega, x) = \sum_{|\omega_i - \omega_j| = \Delta\omega} (\zeta_i e^{-ik_i u\cdot x})^*(\zeta_j e^{-ik_j u\cdot x})Q_d^-(\omega_i, \omega_j, \beta) \tag{16}$$

where Q_d^- is the difference-frequency quadratic transfer function (QTF) for the considered degree of freedom d. Figure 5 shows the QTF for the floater considered in our example. For simplicity, the floater is here assumed to be axisymmetric, so that the QTF represented in Figure 5 is valid for all β. Note that this is not true for the actual INO WINDMOOR 12MW floater.

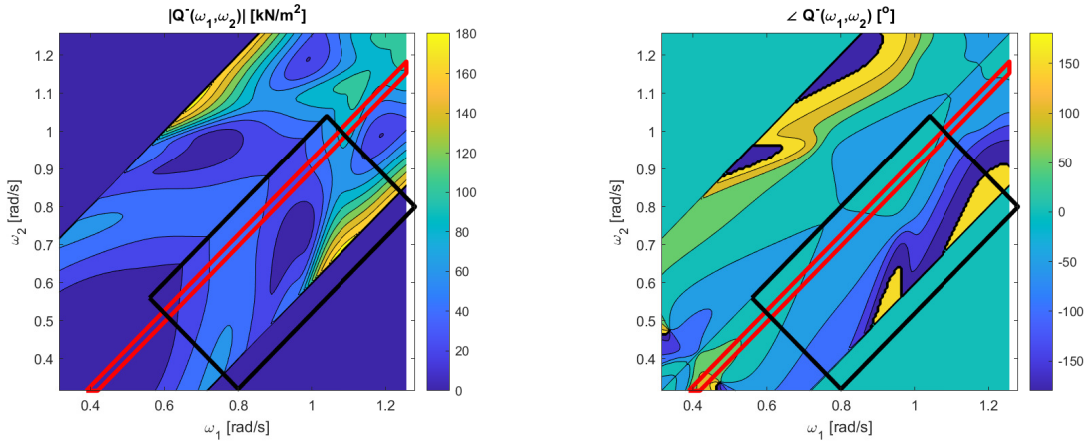

Figure 5. Amplitude (left) and phase (right) of the surge difference-frequency quadratic transfer function of the INO WINDMOOR 12MW floater, obtained from potential flow theory. The red box illustrates difference-frequencies corresponding to the range of eigenfrequencies of the lattice. The black box illustrates mean frequencies at which there is significant wave energy in the chosen sea-state (10 and 90th percentile of wave energy, see Figure 1).

Assuming deep water, and hence a dispersion relationship $\omega^2 = gk$, the load on the floater reads

$$f_d(\Delta\omega, x) = \sum_{|\omega_i - \omega_j| = \Delta\omega} \zeta_i^* \zeta_j e^{i\frac{\omega_i^2 - \omega_j^2}{g} u \cdot x} Q_d^-(\omega_i, \omega_j, \beta) \tag{17}$$

The nodal load[2] vector $F(\Delta\omega)$ for the lattice can then be built by gathering $f_d(\Delta\omega, x)$ for each degree of freedom d and each position x. For example, for a lattice of three structures located at (x_1, x_2, x_3) and with two degrees of freedom each, the nodal load would be obtained by

$$F(\Delta\omega) = [f_1(\Delta\omega, x_1), f_2(\Delta\omega, x_1), f_1(\Delta\omega, x_2), f_2(\Delta\omega, x_2), f_1(\Delta\omega, x_3), f_2(\Delta\omega, x_3)]^\top \tag{18}$$

Once nodal loads are obtained, the modal loads μ_i can be calculated from (8), respectively. They are shown in Figure 4 (upper row) for our example case. Note that by setting $\zeta_i = \zeta_j = 1$, *modal* difference-frequencies QTFs are obtained for the lattice.

From this derivation, and by considering Figure 4, it becomes clear that the amplitude of the modal QTF at a given bi-frequency (ω_1, ω_2) is influenced by three parameters. First of all, (1) the quadratic transfer function at (ω_1, ω_2) represented in Figure 5, appears as a background pattern, providing the strength and phasing of the nodal load on each of the (identical) floaters. On top of that background, (2) *fringes* are observed, that are variations of the modal load over shorter bi-frequency ranges. These fringes are induced by the $(\omega_1^2 - \omega_2^2)u \cdot x$ factor, and thus depend on the wave propagation direction, and the lattice layout. Finally, (3) the projection $F(\Delta\omega) \cdot \phi_i$, which involves the eigenvector/modeshape ϕ_i acts as a uniform multiplying factor over the bi-frequency plane. It is for example noticeable that modes 2 and 7 are clearly less excited than the other ones, due to the fact that the corresponding modeshapes are nearly orthogonal to the wave propagation direction.

[2] Note that the wave load is real due to the Hermitian symmetry of the QTF. Indeed consider a bi-chromatic wave, the sum above reduces to $\zeta_1^* \zeta_2 e^{i\frac{\omega_1^2 - \omega_2^2}{g} u \cdot x} Q^-(\omega_1, \omega_2, \beta) + \zeta_2^* \zeta_1 e^{i\frac{\omega_2^2 - \omega_1^2}{g} u \cdot x} Q^-(\omega_2, \omega_1, \beta)$ which is a sum of complex conjugates, and is then equal to $2\Re[\zeta_1^* \zeta_2 e^{i\frac{\omega_1^2 - \omega_2^2}{g} u \cdot x} Q^-(\omega_1, \omega_2, \beta)]$.

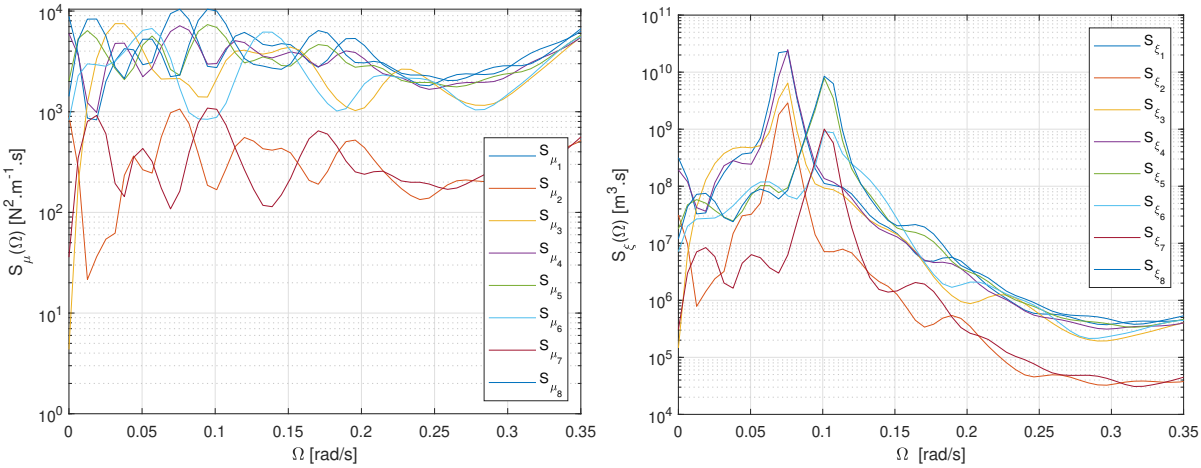

Figure 6. Modal load (left) and response (right) spectra in $H_s = 7$m, $T_p = 10$s (see Fig. 1)

From the modal load μ, modal responses ξ are simply obtained from (13). They are shown in the lower row in Figure 4. It is seen that for the present choice of damping model and damping ratio, the modal response is strongly enhanced at difference frequencies (ω_1, ω_2) matching the eigenfrequencies Ω_i of the mode (resonance). Modal response is relatively smaller for large difference-frequencies in spite of a larger *floater* QTF, as the lattice does not respond significantly to such high frequencies. Note that the properties of the response ξ are very much affected by the assumed Rayleigh damping model and (γ_1,γ_2) coefficients. These assumptions simplify the analysis and enables understanding the mechanisms at play, but there is no indication they are valid.

6. Modal load and response spectra in a sea-state

We now denote Ω, the frequency of the nonlinear wave loading, consistently with Section 3. For a given mode $i \in \{1, ..., n_d\}$ and a given frequency Ω, the spectral density of the modal nonlinear wave load $S_{\mu_s}(\Omega)$ is obtained by integration over all combinations of sea-state components ω and $\omega + \Omega$ that will generate a load at a (difference-) frequency Ω [11, eq (7.99)]:

$$S_{\mu_i}(\Omega) = 8 \int_0^\infty S(\omega) S(\omega + \Omega) |\mu_i(\omega, \omega + \Omega, \beta)|^2 \mathrm{d}\omega \tag{19}$$

Similarly the spectral density of the modal response for mode i, denoted $S_{\xi_i}(\Omega)$ is obtained:

$$S_{\xi_i}(\Omega) = 8 \int_0^\infty S(\omega) S(\omega + \Omega) |\xi_i(\omega, \omega + \Omega, \beta)|^2 \mathrm{d}\omega \tag{20}$$

Spectra of both modal load and response are shown on the left- and right-hand side of Figure 6, respectively, for the sea-state whose spectrum used in the example, and plotted in Figure 1.

Considering S_μ, and leaving aside modes 2 and 7, which are not significantly excited with the given wave propagation direction, it is clear that all other modes are loaded over the whole range of frequencies of relevance for the lattice. Furthermore, large variations of the loading are observed among the modes and across the frequency range (note the y-log-scale of the plots). Modal response is as expected largest near the eigenfrequencies (0.7 and 0.10 rad/s), and then quickly tends to zero. Note however that *linear* wave loads, not included in the present study, are likely to generate a significant modal load and response at frequencies close to 0.63 rad/s.

7. Consequence of applying Newman approximation

In Section 5, we showed how the modal QTF was dependent on the individual floater QTF. Despite the fact that *second-order* potential flow codes are now widely available (such as WAMIT S and Hydrostar), it is still common to consider applying the so-called Newman's approximation, instead of using full QTFs. Newman's approximation consists in approximating the QTF at a bi-frequency (ω_1, ω_2) by the arithmetic mean of its diagonal terms at (ω_1, ω_1) and (ω_2, ω_2):

$$Q_d^-(\omega_1, \omega_2) = \frac{Q_d^-(\omega_1, \omega_1) + Q_d^-(\omega_2, \omega_2)}{2} \tag{21}$$

The historical reason for applying Newman's approximation is that *linear* potential solvers, which are less computationally expensive than their second-order counterparts, give access to the diagonal terms $Q_d^-(\omega, \omega)$ of the QTF, under the denomination wave drift coefficients.

However, a QTF being Hermitian symmetric, its diagonal terms have zero *phase*. So an important bi-effect of Newman's approximation is that the phase information in the QTF, shown on the right hand side of Figure 5, is lost. This has several consequences for the modal loads on lattices. (1) Phase information *between degrees of freedom* of a given floater is lost. If a mode involves e.g. sway and yaw of a given floater, the modal strength will be affected by an error in the relative phases in the nodal load. Furthermore, (2) phase information *between modal loads* will be lost, which can have consequences on quantities of interests that are extracted by combining modal responses. This can be for instance mooring line tensions, estimated from the motions of the floaters. Finally, by construction, (3) Newman's approximation provides more accurate estimates of the *module/real-part* of the QTF near the main diagonal (small difference-frequencies), rather away from it (large difference-frequencies, often of interest for lattices). It implies that Newman's approximation might be less conservative when a QTF exhibits maxima at large difference-frequencies, compared to when such peaks occur near the main diagonal.

The error induced by Newman's approximation[3] can be estimated quantitatively for the example at hand. Denote $\hat{S}_\mu(\Omega)$ the modal load power spectra obtained as outlined in Section 6, but now applying Newman approximation (21) instead of the full QTF Q_d^-. We define the error $\tilde{S}$ in the modal load as

$$\tilde{S} = \frac{\hat{S}_\mu(\Omega) - S_\mu(\Omega)}{S_\mu(\Omega)} \tag{22}$$

$\tilde{S}$ is represented in Figure 7. It is seen to vary from mode to mode and across the frequency range, but with a clear trend being that the error increases with the loading frequency. For the range of frequencies relevant for the lattices considered here (say $\Omega < 0.2$ rad/s), $\tilde{S}$ can reach -40%, meaning that Newman's approximation can lead to modal loads underestimated by 20%. From linearity, the same error would be made on the response spectrum.

Since numerical tools that are practical to use in an engineering context, give access to full QTFs, it is therefore recommended to use them when studying lattices. In many cases, it is recommended to use empirical corrections to the QTF, derived with a cross-bi-spectral analysis [12, Section 4] or least-square based techniques [13, 14]. This has been done for the INO Windmoor 12MW considered here [15], and it was found that for moderate to high sea-states, potential flow predictions generally underestimate the QTF. Such discrepancies are likely to be related to viscous loads, not modelled in potential theory, or to higher than second order potential flow effects.

[3] Since axisymmetry of the floater has been assumed in the present paper, and since quantities of interests due to modal responses have not been investigated, estimates the error induced by points (1) and (2) above are not accessible within the scope of this paper, and we are only considering the effect of point (3).

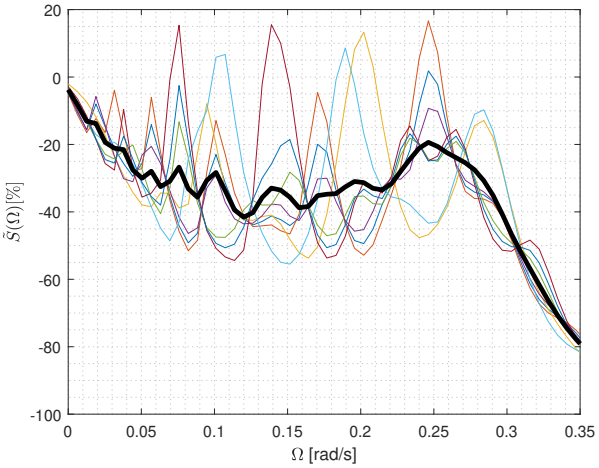

Figure 7. Consequence of applying Newman's approximation on modal load and response spectra. Thin curves refer to each individual mode, with the same color code as in Figure 6. The thick black curve is the average error accross all modes.

8. Conclusion

The present paper introduced modal quadratic transfer functions (QTF) for lattices of marine structures, such as wind parks with shared moorings. The procedure for obtaining modal QTFs consists in performing a nonlinear static (to account for large deformations), a modal analysis of the lattice, followed by the procedure outlined in Section 5. As a results, modal QTFs presented in Figure 4 are obtained. Their features have been explained in details in Section 5. For the example used in the paper, that is a grid-type of lattice with four floaters, it has been shown that applying Newman's approximation could lead to an significant underestimation the modal loads.

The modal *response* of the lattice has also been derived, assuming a Rayleigh damping model which led to uncoupled modes, and given the choice of Rayleigh coefficients, to resonant modes. This enabled understanding the mechanisms at play, but there is no indication that this damping model is applicable for shared mooring systems. If shared lines induced a large amount of damping, resonance might be avoided, even under wave loading occurring at the eigenfrequencies of the lattice.

Further work is ongoing to model and quantify damping. This will enable extending the frequency domain analysis to study lattice responses, and derived quantities of interest such as tensions in mooring lines, and absolute/relative excursion of floaters. Understanding the role of specific modes on these quantities of interest is of interest for design.

Finally, it should be stressed that the present paper only focused on second-order wave loads, of interest because they occur at typical eigenfrequencies of lattices. Wind loads and *linear* wave loads, usually significantly larger in magnitude, should of course be included in the dynamic analysis of a lattice.

9. Acknowledgments

This research has been funded by the Research Council of Norway through project 326654 CYBERLAB KPN, a collaboration between SINTEF Ocean, NTNU, University of Aarhus, Equinor, Aker Offshore Wind, APL Norway, Sevan SSP and Delmar Systems. The author wishes to acknowledge the contribution of students Claire Monin and Clément Morhain who have performed preliminary studies that led to the present work, as part of their stay at NTNU and SINTEF, respectively.

References

[1] Patrick Connolly and Matthew Hall. Comparison of pilot-scale floating offshore wind farms with shared moorings. *Ocean Engineering*, 171:172–180, January 2019.
[2] Guodong Liang, Karl Merz, and Zhiyu Jiang. Modeling of a Shared Mooring System for a Dual-Spar Configuration. In *Volume 9: Ocean Renewable Energy*, page V009T09A057, Virtual, Online, August 2020. American Society of Mechanical Engineers.
[3] Samuel Wilson, Matthew Hall, Stein Housner, and Senu Sirnivas. Linearized modeling and optimization of shared mooring systems. *Ocean Engineering*, 241:110009, December 2021.
[4] Patrick Connolly. Resonance in Shared Mooring Floating Offshore Wind Turbine Farms. Master's thesis, University of Prince Edward Island, 2018.
[5] Marek Goldschmidt and Michael Muskulus. Coupled Mooring Systems for Floating Wind Farms. *Energy Procedia*, 80:255–262, 2015.
[6] Matthew Hall and Patrick Connolly. Coupled Dynamics Modelling of a Floating Wind Farm With Shared Mooring Lines. In *Volume 10: Ocean Renewable Energy*, page V010T09A087, Madrid, Spain, June 2018. American Society of Mechanical Engineers.
[7] Matthew Hall, Ericka Lozon, Stein Housner, and Senu Sirnivas. Design and analysis of a ten-turbine floating wind farm with shared mooring lines. *Journal of Physics: Conference Series*, 2362(1):012016, November 2022.
[8] Ozan Gözcü, Stavros Kontos, and Henrik Bredmose. Dynamics of two floating wind turbines with shared anchor and mooring lines. *Journal of Physics: Conference Series*, 2265(4):042026, May 2022.
[9] Ericka Lozon and Matthew Hall. Coupled loads analysis of a novel shared-mooring floating wind farm. *Applied Energy*, 332:120513, February 2023.
[10] Carlos Eduardo S. Souza, Petter Andreas Berthelsen, Lene Eliassen, Erin Bachynski-Polić, Espen Engebretsen, and Herbjorn Haslum. Definition of the INO WINDMOOR 12 MW base case floating wind turbine. SINTEF Ocean Report OC2020 A-044 v1.2, SINTEF Ocean, January 2021.
[11] Bernard Molin. *Offshore Structure Hydrodynamics*. Cambridge University Press, first edition, January 2023.
[12] Thomas Sauder. Empirical estimation of low-frequency nonlinear hydrodynamic loads on moored structures. *Applied Ocean Research*, 117:102895, December 2021.
[13] Tim Bunnik, René Huijsmans, and Yashiro Namba. Identification of quadratic responses of floating structures in waves. In *The Sixteenth International Offshore and Polar Engineering Conference*. International Society of Offshore and Polar Engineers, 2006.
[14] Øyvind Ygre Rogne, Nora Haug, and Rolf Løken. An Improved Method for Model Test Based Identification of Drift Coefficients and Damping for Floating Platforms. In *Offshore Technology Conference*, 2016.
[15] Nuno Fonseca, Maxime Thys, and Petter Andreas Berthelsen. Identification of wave drift force QTFs for the INO WINDMOOR floating wind turbine based on model test data and comparison with potential flow predictions. *Journal of Physics: Conference Series*, 2018(1):012017, September 2021.